Supplementary Materials for

Deposition, exhumation, and paleoclimate of an ancient lake deposit, Gale crater, Mars

J. P. Grotzinger,* S. Gupta, M. C. Malin, D. M. Rubin, J. Schieber, K. Siebach, D. Y. Sumner, K. M. Stack, A. R. Vasavada, R. E. Arvidson, F. Calef III, L. Edgar, W. F. Fischer, J.A. Grant, J. Griffes, L. C. Kah, M. P. Lamb, K. W. Lewis, N. Mangold, M. E. Minitti, M. Palucis, M. Rice, R. M. E. Williams, R. A. Yingst, D. Blake, D. Blaney, P. Conrad, J. Crisp, W. E. Dietrich, G. Dromart, K. S. Edgett, R. C. Ewing, R. Gellert, J. A. Hurowitz, G. Kocurek, P. Mahaffy, M. J. McBride, S. M. McLennan, M. Mischna, D. Ming, R. Milliken, H. Newsom, D. Oehler, T. J. Parker, D. Vaniman, R. C. Wiens, S. A. Wilson

*Corresponding author. E-mail: grotz@gps.caltech.edu

This PDF file includes:

Supplementary Text
Figs. S1 to S10
Tables S1 and S2

Supplementary Text

Age of Aeolis Palus From Crater Count Statistics

The age of Aeolis Palus can be estimated via its cumulative crater statistics. Two areas covering a total of 570 km2 approach the expected production population (*78*) at diameters over 200 m (Figure S1A) and yield an interpreted age in the middle of the Hesperian for a modeled absolute age in the range of ~3.3 to 3.1 Ga (*56*). Similar distributions are observed for neighboring Sharp crater where aqueously influenced landforms are observed (*79*). Importantly, craters >200-400 m in diameter are uniformly distributed across Aeolis Palus (Figure S1B, C) and their survival constrains any erosion and (or) deposition after the middle of the Hesperian to ~20-40 m. This is based on the erosion or burial required to remove the craters assuming a depth-to-diameter ratio of 0.2 if they are primary and 0.1 if they are secondary craters, respectively (*80*). Although local erosion may exceed this amount, more significant widespread erosion or deposition would lead to gaps in the observed distribution of larger craters.

Chronology of Exploration and Rover Operations

Between sols 21 (first drive of the mission) and 323, Curiosity drove 841 m across bedrock of the Bradbury group, including the Yellowknife Bay formation. From sols 324 to 700 Curiosity drove 7,800 m to the southwest from Yellowknife Bay to the southern edge of the Zabriskie Plateau, stopping along the way to make observations along the way of the Bradbury group (Figure 1). From sol 392 to 401 the rover stopped to make a number of densely spaced observations at the Darwin outcrop, and then again at the Cooperstown outcrop between sols 440 and 443. Between sols 571 and 631 the Kimberley formation (Bradbury group) was studied in detail, including drilling between sols 609 and 629. On Sol 706 Curiosity crossed the boundary between the Bradbury group and Murray formation (Mt. Sharp group), descending into Hidden Valley. The sand in this valley was too loose to be traversable, so the rover exited along its ingress path, drove up and around Hidden Valley to the north, and then into Amargosa Valley on Sol 743, again crossing the Bradbury group/Murray formation contact. On Sol 753 Curiosity arrived at the Pahrump Hills outcrop.

Drilling and sampling occurred immediately after arrival (Confidence Hills target, sols 755-765). Subsequently the outcrop was studied in two looping passes; the first was dedicated to reconnaissance and remote sensing (Sols 780-797), the second was dedicated to contact science at key parts of the outcrop identified during the first loop (Sols 805-862). Further drilling and sampling was completed after the second loop (Mojave target, sols 867-888; Telegraph Peak, sols 903-922).

Mapping Methodology, Orbitally Striated Outcrop (OSO)

Individual striations were identified as thin (<2 m), low-albedo, linear features that laterally extend a minimum of 5 m within the OSO. A total of 741 striations were identified and mapped as vectors in ArcGIS, and the strike directions were calculated from the endpoints of each line. The strike measurements were plotted in a rose diagram

with 10 degree bins. The dominant strike direction is N65E, with 26% of measurements between 60 and 70 degrees.

Exposure of OSO in Topographic Depressions

The question arises as to whether the OSO rocks have been deposited within topographic lows eroded into the more resistant strata that form the upper surface of Aeolis Palus in this area. Alternatively, the OSO rocks were exhumed by eolian erosion of overlying strata. The striations: (1) bear no obvious relationship to the morphology of the depressions in which they occur, (2) locally completely surround isolated mesas with no variation in their orientation, and (3) appear to terminate sharply where they abut strata occurring at locally higher elevations. These observations—that their trend is independent of the geometry of the topography around them—imply that the OSO records exhumation of buried strata rather than strata later infilling topographic lows. Finally, rover observations of clinoform sandstones not associated with OSO, and seen in the bedrock exposed along valley walls, as well as on topographic highs, support this inference.

Diagenetic Features in Murray formation at Pahrump Hills

Diagenetic features are observed in Murray formation outcrops exposed at Pahrump Hills and the broader Hidden Valley-Amargosa Valley network. Dendritic forms are composed of densely spaced 1-3 mm diameter spherical to ellipsoidal bumps, that cluster to form elongate and irregular chains that range in length from 1 to 8 cm (Figure S3A). These are interpreted as concretions which grew within the finely laminated mudstone as cement precipitated within the sediment pore network; data do not allow us to determine if they formed prior to or post compaction of the host sediment.

Small prismatic crystals (or their pseudomorphs) with tapered ends are present at the Mojave target (Figure S3B). Prismatic crystals are lighter than the host rock and make up about 20% of the rock. Most prisms are 0.2 mm wide with apparent lengths from 0.5 to 1.5 mm with a mode of 1.2 mm. Broken parts of the outcrop show that they extend beneath the outcrop surface and are a feature of the rock itself. Prismatic crystals are interpreted to have grown within the sediment due to their highly elongate geometry and isotropic orientation. The lack of disruption to the fine, primary lamination further suggests these crystals grew interstitially, so that sediments were not displaced. The morphology and light tone of the tapered, prismatic crystals is most consistent with diagenetic salts such as calcium sulfates. However, elemental and mineralogic data provide no evidence for any authigenic or alteration phase sufficiently abundant to explain their textural abundance. Thus, the most likely explanation is that the diagenetic mineral has been leached, leaving pseudomorphs expressed by residual intergranular porosity.

Light-toned veins filled with late diagenetic minerals pervade most strata exposed in the Hidden Valley-Amargosa valley network. They are most apparent in the finely laminated mudstone facies just beneath the contact with the thickly laminated facies at the Pahrump Hills outcrop (Figure S3C). Veins vary from <1 mm to several cm in width and extend for at least several meters, forming complex patterns. Geochemical data indicate that these veins are composed of calcium sulfate. The light-toned veins are very

similar to the sulfate filled-fractures described from the Yellowknife Bay formation where XRD data show the presence of anhydrite and bassanite. Similarly, overpressured fluids may have fractured rocks, particularly near facies boundaries where gradients in porosity and permeability may have existed (*5, 74, 81, 82*).

<u>Estimation of Lamina Thickness For Thinly Laminated and Thickly Laminated Facies</u>

We used wavelet analysis to characterize the natural variability of the observed lamination by grayscale pixel intensity for the regions orthogonal to bedding. Thin (by *m*) matrices were extracted from the image, converted to grayscale and pixel intensity was summed along bedding to provide time/depth-varying signals for the different regions of interest. The signals clearly resolve and contain characteristic peaks that capture thicknesses due to differential weathering of the laminae that are readily observable in the Mastcam images. The data were linearly de-trended and normalized to the mean. No further filtering or stretching of the image data was done. Wavelet analysis using a Gaussian "mother" wavelet was completed and a power spectrum computed by integrating the wavelet energy function over all locations of the signal. The spectra for the outcrop of thinly laminated facies (Figure S5A, B) displays notable humps at ~0.25 cm, which correspond to the smallest thickness of observable laminations in the Mastcam image. Corrected for viewing angle, this value becomes ~0.22 cm. The spectra of the thickly laminated facies (Figure S5C) display a peak at a larger characteristic thickness, ~ 0.5 cm (no viewing angle correction was required for this image). Other peaks in the spectra are tied to changes in either the aspect or dust content of the outcrop and cannot be confidently interpreted as nested signals within the strata.

A complementary approach to examining the laminae is computing thickness distributions from the image signals. We did so by identifying local peaks in the signals and obtaining the first differences between the peak locations. The empirical mean and standard deviations of the distributions are shown in Table S2, kernel density estimates of the thickness distributions are shown in Figure S6. Most notably, the distributions for both outcrops of laminites at Pahrump and Hidden Valley are right-skewed. The data are consistent with gamma distributions (which describe the sum of exponentials), but also heavy-tailed distributions (e.g. Pareto, log-Normal); this is strongly suggestive of a stochastic depositional process, e.g. (*49*).

There are caveats in this analysis. The results of spatial frequency analyses of Mastcam images may be somewhat spurious owing to a number of processing factors associated with the imaging system. Specifically, the Bayer Color Fiilter Array reduces spatial frequency content between 0.33 and 0.5, the two dimensional Bayer interpolation (demosaicing) spreads frequencies around the interpolator kernel (5x5 pxls ~ 0.2 spatial frequency), and JPEG compression specifically modifies high spatial frequencies between 0.125 and 0.5 (by both the processes of requantification and zero truncation). Once transmitted to the ground, our data go through a decompression algorithm that, as with many JPEG decompression algorithms, treats the expansion of requantized and/or trucated values using psychovisual parameters (that may also further modify the frequency domain data). The images used in this analysis were further modified by consumer image processing software (point matching and spatial warping to permit mosaicing, also impacting spatial frequencies). Two points about these issues can

be made. First, many of the problems can be avoided by returning the data losslessly (rather than as JPEG files), and special processing can improve the frequency relationships, while relying on the U. S. Air Force's definition of resolution (the spatial frequency at which 50% contrast is attained). Secondly, the layering described is easily seen in visual inspection of the images, and spatial sampling of those visual inspections can be used to validate the frequency analyses.

Laminated Mudstone Facies: Alternative Eolian Depositional Mechanisms

One alternative interpretation of the finely-laminated mudstone facies involves the passage of eolian impact ripples to form fine "pinstripe" lamination. Pinstripe stratification is common on Earth (*14, 83*), and has been recognized previously on Mars, where medium grained sulfate-rich sandstones were observed in the Burns formation of Meridiani Planum (*84*). Low-angle foreset stratification, inverse grading, and low angles of climb characterize pinstripe stratification; none of these are observed in the Pahrump Hills laminated mudstone facies. Furthermore, accretion of thick intervals of horizontally-bedded pinstripe lamination is unknown on Earth; in dry eolian systems a few decimeters of pinstripe lamination is often followed or preceded by thick sets of large-scale cross stratification (*52*). That same relationship is also true for damp systems, but here the pinstripe stratification represents moist interdune depressions that are subject to desiccation and thus leave behind telltale sediment filled cracks. Desiccation cracks are not observed in the laminated mudstone facies, which contrasts with the pinstripe lamination seen in the Burns formation at Meridiani (*85*). Finally, the grain size of the finely laminated mudstone facies is so fine—below the resolution of the camera, at 60-70 microns—that this may have limited the formation of eolian impact ripples. Eolian impact ripples are typically formed of sand sized particles, with the impact ripple stability field narrowing abruptly at grain sizes less than 200 microns, and closing entirely for sediments less than 100 microns (*86*). On Mars, with a lower gravitational acceleration and decreased atmospheric pressure, the shape and position of the ripple stability field is likely to shift. It is possible that impact ripples could form with 50-60 micron sediment based on theoretical calculations (*87*). However, even for this adjustment, the stability of impact ripples on Mars is right at the boundary of what we estimate the maximum grain size to be for Pahrump sedimentary rocks. Therefore, we question that this could explain such great thicknesses of mm-scale lamination (several meters) that are unknown even on Earth where eolian impact ripples are stable for a broad range of grain sizes.

A different eolian process that could account for mm-scale lamination could be adhesion of dry, fine sediments to a wet or damp surface, promoted by capillary wicking of groundwater. Known as "adhesion ripples", these features are loose clumps of sediment that migrate through sticking and release of sediment, and propagate in mode similar to ripples (*88, 89*). Rather than involving saltation-avalanche dynamics, adhesion ripples form through sticking of sediment to droplets of moisture. Therefore, these features have a crinkly and lumpy shape, and the resulting stratification is typically irregular and highly discontinuous. Adhesion ripples thus cannot explain the plane-parallel nature of the Murray lamination, nor its regularity or substantial lateral continuity.

A related, but morphologically different class of structure produces "adhesion lamination" (*89, 90*). In this case, sediment adheres to a damp surface not marked by

adhesion ripples or impact ripples, possibly due to a lower degree of wetness. The bed is generally smooth with a crinkly texture not much exceeding grain roughness. Resulting stratification is fine, but still crinkly, with greater lateral continuity as compared to adhesion ripple stratification. In some cases, adhesion lamination has been observed as parts of drying upward sequences, transitional between subaqueously deposited strata and subaerially deposited large-scale dune strata (*89*). However, compared with pinstripe lamination, adhesion stratification is even more restricted in the rock record and rarely forms thicknesses greater than a few cm. A balance must be achieved so that there is just enough moisture to trap sediment, and not too little that all sediment bypasses the surface, or not so much that adhesion ripples form, or the environment becomes submerged to form playa or perennial lacustrine facies. On Earth, this balance is rarely sustained for long, resulting in cm-scale to dm-scale thicknesses of adhesion lamination. It is not obvious how this balance would have been stabilized more for Mars, therefore, we discount adhesion lamination as a process to generate meter-thick sequences of finely laminated mudstone.

Compaction of Gale Crater Strata

The compaction of sediments to progressively lose porosity is an inevitable consequence of the accumulation of thick successions of strata. The strata of Gale crater are expected to show the effects of compaction, including vertical deflection related to lateral gradients in thickness and lithology. Here we examine this effect as a way to help explain the orientation of bedding, observed from orbit in HiRISE images, which gently dips away from Gale's central peak (*55*). These dips of 3° $\pm$2° are observed in strata of the hematite unit (*11*) and overlying sulfate-bearing strata (*10*) (Figure 1).

Compaction is part of diagenesis and the process of lithification. For sediments compacted under self-weight the profiles show an exponential decrease in porosity, known as Athy's law (*91*). Sediments are originally deposited as an open framework of particles with pore space usually filled with water, and less commonly air. As sediment progressively accumulates the effect of increased loading is to increase particle-particle stresses, resulting in adjustment and shifting of particles to cause porosity reduction and more efficient packing of particles. The initial porosity of sediments depends on lithology, with shales and mudstones having the highest initial values and sandstones and gravel showing progressively lower values.

Physical compaction of sediments within sedimentary basins can be modeled using porosity-depth relationships derived from databases of empirical measurements from different sedimentary basins on the Earth (*91-93*). These porosity-depth curves are most strongly dependent on sediment lithology and grain size (*91, 94, 95*), but also vary between basins due to fluid overpressure (*95*), sedimentation rates and geologic age (*96*), and early cementation processes (*97*). The porosity-depth dependence within a mono-lithologic column of sediment is most simply modeled as an exponential function following Athy's law (*91*):

$$\phi(z) = \phi_i e^{-cz} \qquad\qquad\qquad (1)$$

Where $\varphi(z)$ is the porosity at burial depth z, φ_i is the initial porosity, and c is an empirical constant based on the sediment lithology. This empirical relationship has been

shown to work in a wide variety of basins on Earth and φ_i and c parameters for distinct lithologies are reported in (*98*). In order to apply these empirical models to Mars, we will assume that the largest effect is the difference in the gravitational acceleration, and otherwise take the empirical constants for the lithologies most similar to those observed by Curiosity at Gale crater (conglomerate, sandstone, siltstone, and shale) (*98*). Based on a semi-analytical solution for porosity (*99*), the gravitational constant factors into the exponent term, so we modify Athy's Law as follows:

$$\phi(z) = \phi_i e^{-\left(g_{Mars}/g_{Earth}\right)cz} \tag{2}$$

The percent of physical compaction of a sediment column in the absence of other effects can then be calculated as the initial percent of solids (1- φ_i) over the final percent of solids (1- $\varphi(z)$), and this calculation of compaction with depth is shown in Figure S7.

As shown in Figure S7, significant sediment compaction occurs during the first ~1 km of burial of the sediments, with the percent compaction depending on the lithology of the sediments and increases with decreasing grain size. Based on the discussion of the expected depth to basement in the northern portion of the Gale Crater moat (Figure S9, S10), there could be as much as ~1.1 to 2.1 km of sediment between the post-impact surface and the current floor of the crater. Furthermore, based on exposed stratigraphy on Mount Sharp, there was at least ~1 km of sediment above the current floor of the crater that has since eroded away (Figure 8), so significant compaction should be expected for the Murray formation and any underlying sediments. Near the center of the crater, however, presence of relief associated with the central peak would create systematically less sediment thickness and burial depths, thereby resulting in differential compaction that increases with distance from the central peak. This sediment compaction will create a dip in initially planar beds that should contrast with and be measureable relative to the rigid central peak of the crater. Indeed, planes measured on beds within the hematite ridge and sulfate units on Mount Sharp show dips of 3°±2° away from the central peak (*55*). Here, we accept those values though they have not been independently confirmed.

Figure S8 shows expected dip angles for bedding observed 30 km away from the rigid central peak (approximately the distance to the exposed hematite unit, see Figure 8) based on compaction of sediments between the ridge and the crater basement. Rover observations of strata below the hematite ridge indicate that mudstone lithology may dominate the Murray Formation; if so, significant compaction would be expected (see red and green highlighted boxes). Given the possibility of at least 1-2 km of strata beneath the level of the hematite unit, Figure S8 indicates the measured bedding planes of 3°±2° away from the central peak are consistent with sediment compaction within the northern moat of Gale crater relative to the rigid central peak.

Sediment Supply from Gale Crater Walls
Gale Crater has been classified (*100*) as retaining the characteristics of a fresh impact crater involving a rough ejecta blanket, raised rim, and hummocky interior walls (criteria proposed by (*101*)), but some crater wall and rim erosion has occurred: the lower crater wall slopes are blanketed with waste material and sediment mantles the crater floor. To calculate possible erosion and/or deposition within Gale, we utilize two

independent approaches—a comparison of Gale's rim height, and a comparison of crater depth with fresh crater values using empirical power law relationships (*63*). Further, we describe a simple geometric model that shows how rim erosion can be explained by a simple model of crater-wall backwasting as coarse debris (not wind deflation), which would lead to significant aggradation of the crater floor. These estimates of sediment fill are further supplemented by the localized watershed-generating erosion of the Peace Vallis catchment, as discussed in the following section.

Estimate using rim height. Figure S9A and S9B show typical profiles going north-south and east-west, respectively, across the crater. These data were collected from a High Resolution Stereo Camera (HRSC)-derived topographic map at a resolution of ~50 m/pixel, and supplemented with Mars Orbiter Laser Altimeter (MOLA) data at ~100 m/pixel. Our analysis of 24 individual measurements of Gale's southern rim, shows an average measured rim height of 0.58 ± 0.41 km. (*63*) reports:

$$h_i = 0.025(D_c)^{0.82} \hspace{4cm} (1)$$

where h_i is the height of the rim minus the height of the adjacent plain beyond the ejecta blanket (T- RB, in Figure S9) and D_c is the crater diameter. This relationship is nearly the same as that reported by (*102*) and matches the data in (*103*). Based on 12 long profiles, all which cross through Gale's central peak, the diameter of Gale is 157 ± 9 km. From equation (1), the estimated fresh rim height (h_i) would have been 1.6 km. This implies an erosive lowering of ~1 km on average for the Gale crater rim. Based on the preservation of the ejecta blanket we think this number is likely too high. Furthermore, Gale struck at the Martian topographic dichotomy boundary, possibly during relatively wet times, which may have influenced the initial raised rim height (h_i). The possible overestimate here may be offset by the lack of quantitative accounting of sediment shed in making the Peace Vallis catchment, discussed further below.

Estimate using crater depth. The profile analysis of Gale crater yielded a crater depth (lowest point to rim height) of 3.1 ± 0.7 km. For complex craters between -40° to $+40^o$ latitude, (*63*) reports the relationship between crater depth (D_i) and diameter (D_c) for complex craters as

$$D_i = 0.229 \, (D_c)^{0.567} \hspace{0.3cm} (\text{"fresh"}) \hspace{3cm} (2)$$

$$D_i = 0.280 \, (D_c)^{0.57} \, (\text{deepest}) \hspace{3cm} (3)$$

This leads to a predicted depth of 4.0 km for "fresh" and 5.0 km for "deepest". "Fresh" craters are defined (*63*) as those having light to moderate modification and an ejecta blanket surrounding its rim, and "deep" craters as the deepest 25 craters within a $2^{1/8}D_c$ bin. Comparison of the measured and expected depth of Gale indicates that it is too shallow by 1.1 to 2.1 km, which could be explained by some combination of rim erosion or crater infilling. If our crater-rim-erosion estimates of ~ 1 km are correct, for example, then this would indicate a deposit $0.1 - 1.1$ km on top of the post-impact crater floor. However, smaller estimates of crater rim erosion would lead to proportionally larger

estimates of deposit thickness, with a maximum deposit thickness of 2.1 km for pristine crater rims. As mentioned above, the complexity of the crater site adds uncertainty to these numbers. In particular, impact on the dichotomy boundary may predict even greater values for the depth to the post-impact surface of the northern crater than what are estimated using equations 2 and 3.

Figure S10 illustrates a simple geometric model of how rim lowering caused by back stepping of the crater wall produces significant sediment production to the crater floor. The original fresh crater depth is labeled D_i. Initial rim top is labeled IT and current rim top is T. The local rim height at the initial and current stage are labeled h_i and h_f respectively. For simplicity, we assume that rim height decline is caused by slope parallel retreat. The horizontal back stepping distance, W, is

$$W = (h_i-h_f)/\tan\alpha \tag{4}$$

The back step distance normal to the slope, L_n, is

$$L_n = W \sin\alpha \tag{5}$$

The inclined length (of the back step area), L, is

$$L = D_i/(\sin\alpha) \tag{6}$$

Hence, the cross-section area, A, removed as a consequence of the back step is

$$A = W \sin\alpha \ (D_i/(\sin\alpha)) = W \ D_i \tag{7}$$

We assume that alpha in Figure S10 for the topography immediately after impact is best estimated from the exposed bedrock walls of the crater. We first mapped the location of the transition from bedrock to crater wall deposits (e.g. talus, colluvium) along each of our long profiles using MRO Context Camera imagery. Then, using only the elevation data, where we observed intact bedrock we calculated the slope over 100 m intervals. The average inner rim slope was 0.21 ± 0.11, or an alpha of 11.8 degrees. Using the results of the topographic analysis of Gale and the power law relations for estimated "fresh" conditions, we find that the back stepping distance, W, is estimated to be 4.8 km, which leads to a normal slope erosion of 1 km. The inclined slope length is 19.6 km (for $D_i = 4$ km) and 24.5 km (for $D_i = 5$ km). The cross sectional area correspondingly becomes 19.2 km^2 and 24 km^2.

If we assume a uniform radial erosion rate, then the total volume of sediment that would be delivered to the crater floor, V, is

$$V = 2pR \ W \ D_i \tag{8}$$

Which for the 78.5 km radius (R) of Gale gives 9,470 km^3 for 4 km D_i and 11,837 km^2 for 5 km D_i. If the density of the eroded and deposited material is the same, such that

volumes can be directly compared, when spread over an area of 18,250 km^2, this equates to 0.5 to 0.6 km of deposition. The area over which sediment was deposited was assumed to be the crater floor area extending between the crater rim and central peak, and was calculated from the mapped planform area of the entire crater floor (using HRSC data in ARCGIS), excluding the bedrock walls, minus the area mapped to be the original central peak (the central peak (CP) can be see in the long profile of Gale in Figure S9 A and B). As the crater is bowl-shaped, the actual depositional area changes as the crater becomes more infilled, but we assume these errors are within the noise for the estimates made here. By independently comparing both Gale's rim height and crater depth with fresh crater values using empirical relationships, we find that Gale could be infilled by ~0.5 to 2 km. On average, it is shallower than expected for a crater of its size and its rims are muted, suggesting a significant local sediment source.

We consider 1.5 km to be a reasonable alternative to the very conservative estimate (a few hundred meters) shown in Figure 8, for the thickness of sediment between the post-impact crater floor and the present day crater floor.
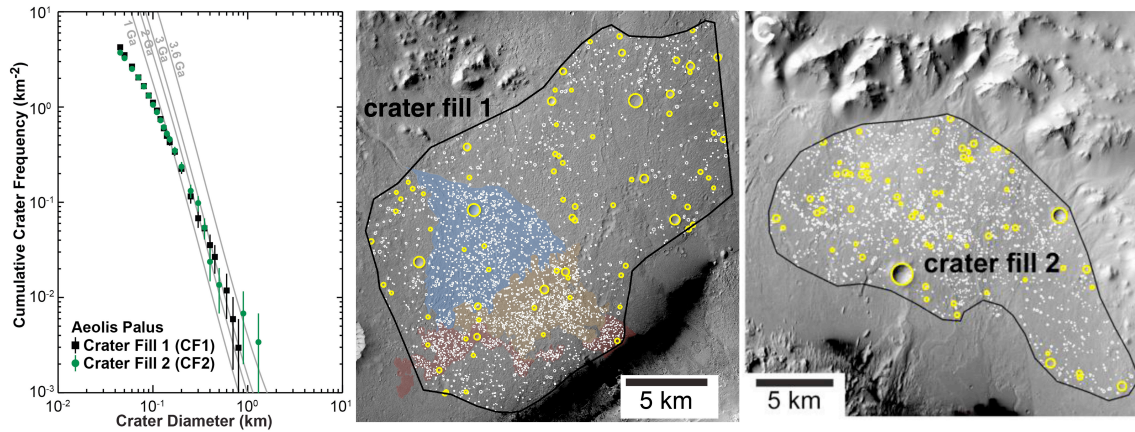
Supplementary Figures

Fig. S1

A) Cumulative (left) crater size frequency distributions for Crater Fill area 1 (CF1, includes the traverse of Curiosity) and Crater Fill (CF2) on Aeolis Palus indicating a production population of craters >200-400 m in diameter and yielding a modeled age of ~3.3-3.1 Ga (middle of the Hesperian). B) CF1 (center) and (C) CF2 (right) cover surfaces of fairly uniform texture and crater density on Aeolis Palus and both areas include water lain deposits (e.g., the Peace Vallis fan unit and adjacent light-toned fractured unit, light blue and brown, respectively in (B)) as well as surfaces retaining higher densities of smaller craters ("cratered surface" unit, (ref. 11) CS in (B)). The area between CF1 and CF2 is characterized by high standing remnants of a deposit that differs in morphology and was therefore excluded. Error bars reflect +/- 1/N0.5 (N= number of craters; A=area). Larger craters (≥ 200 m in diameter, yellow circles) are distributed uniformly across CF1 and CF2 and their survival indicates denudation after the middle of the Hesperian was limited to no more than ~20-40 m. To improve readability of the maps, only craters larger than ~60 m in diameter are shown on surfaces outside of the Peace Vallis alluvial fan unit, the light toned fractured unit, and "cratered unit" (see (*5*) for unit definitions). North towards top.
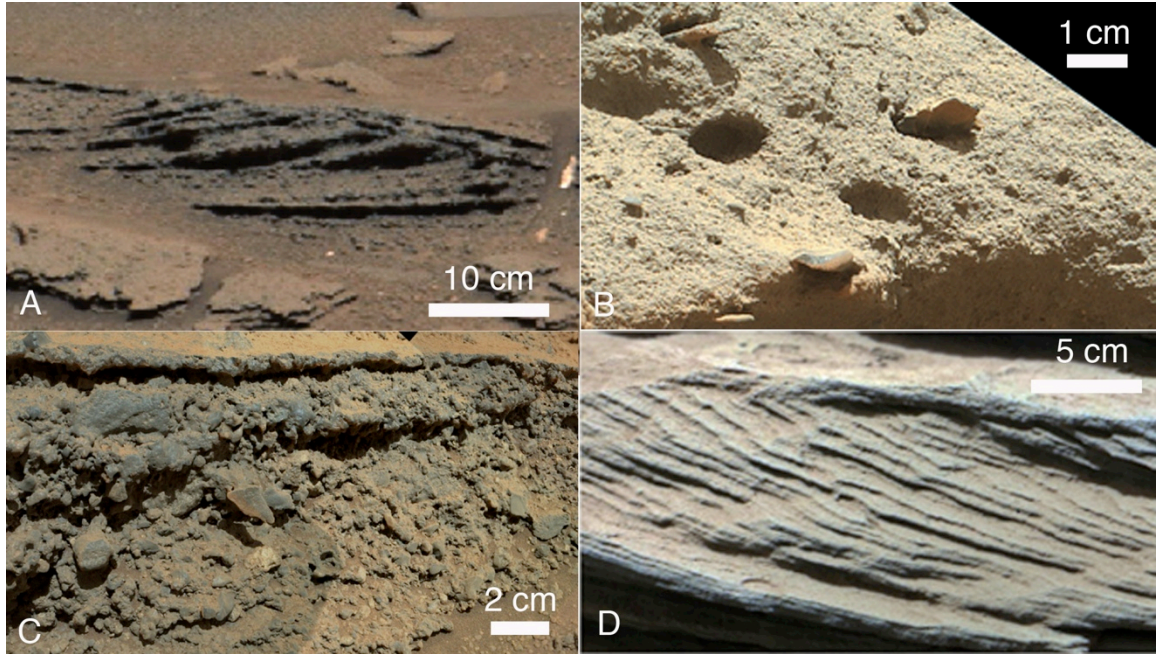
Fig. S2.

Representative sedimentary facies of the Bradbury group. All views are cross-sections of beds. A) Trough cross-bedded granule-pebble conglomerate, Junda outcrop ("Kylie" locality, see Figure 1). Mastcam image acquired on Sol 602; B) Pebbly sandstone, Cooperstown locality. These are characteristically weakly stratified and show preferred clast orientation. MAHLI focus merge product 0443MH0003290000200185R00; C) Poorly stratified, poorly to moderately well sorted coarse pebble conglomerate, JumJum outcrop ("Kylie" locality, see Figure 1). Mosaic of MAHLI images 0550MH0003540000201601C00, 0550MH0003520000201602C00, 0550MH0003530000201600C00; D) Trough cross-stratified very fine grained, very well sorted sandstone, west Amargosa valley outcrop. Note that cross-stratification is defined by very fine pinstripe laminae, suggestive of the migration of impact ripples across the lee face of small eolian dunes. Grain size is constrained by what the Mastcam M100 can resolve, on the order of 0.5-1.0 mm at an offset distance of 2 m; pebbles are not observed in these sandstones. This cross-stratification is inferred to have formed by eolian impact ripples migrating across and up the lee side of a small eolian dune. Mastcam image acquired on Sol 746.
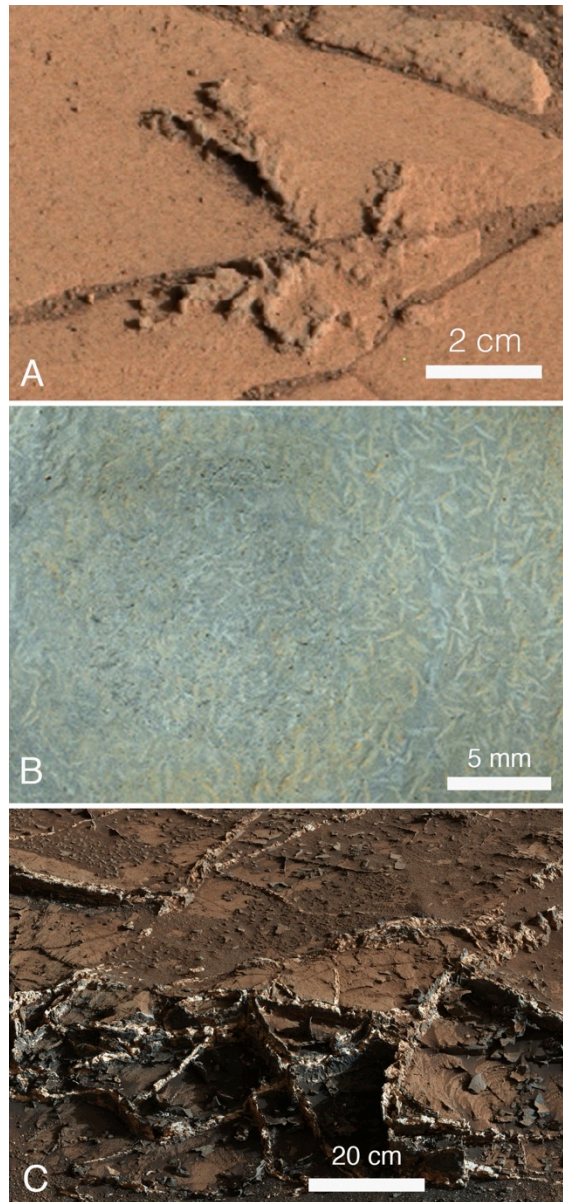
Fig. S3

A) Diagenetic dendrite structures, likely concretions, formed in the mudstone formed by mineral precipitation from pore fluids. Mastcam image acquired on Sol 753. B) Crystal pseudomorphs formed in the finely laminated mudstone by diagenetic mineral precipitation, morphologically similar to gypsum, and suggest evaporative concentration of pore fluids. Illuminated by white light LEDs at night, this is a portion of a mosaic of MAHLI focus merge products, 0809MH0001710000300942R00, 0809MH0001710000300944R00, 0809MH0001710000300946R00, and 0809MH0001710000300948R00. C) Late diagenetic veins represent mineral precipitation in fractures that cross cut all rocks units studied by Curiosity to date, up to and including the Murray formation at Pahrump Hills. Mastcam image acquired on Sol 929.

Fig. S4

Ordering of facies at Panamint Butte. For location and stratigraphy see Figure 5. Sandstones and conglomerates of the Bradbury group dip southward and are overlain by a unit whose recessive expression, massive appearance and light tone is identical to that of the finely laminated mudstone that defines the Murray formation at Pahrump Hills, observed from a similar distance. Arrows point to intercalated resistant beds that are also characteristic of the Murray formation mudstone at Pahrump Hills (see Figure 7A). This suggests interfingering of facies along a delta foreslope as shown in Figure 5. This occurrence of mudstones above conglomerate also is observed at Pahrump Hills (section 6, Figure 5).
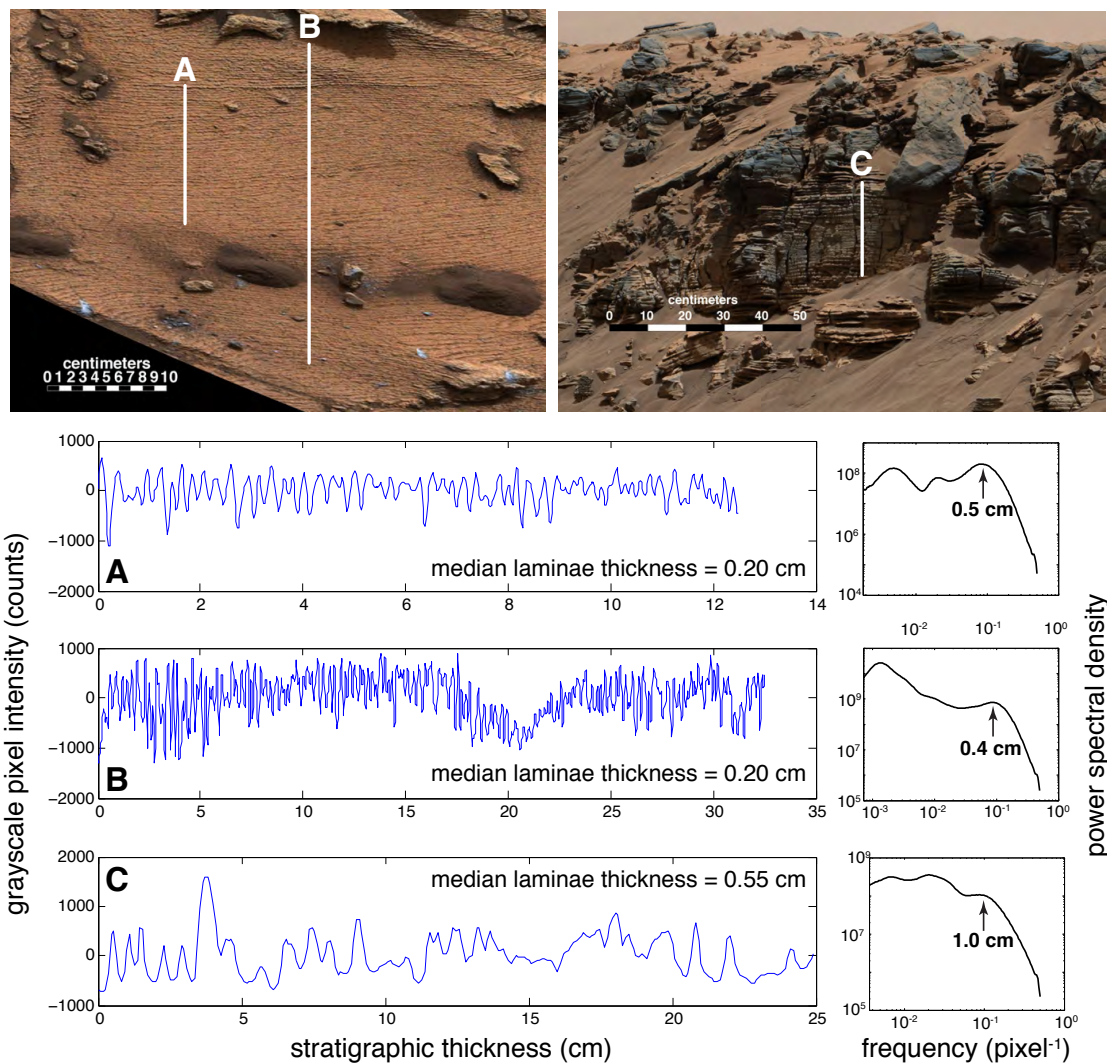
Fig. S5

Lamination was measured from outcrops of the Murray formation (Pahrump Hills member) shown in Figure 7B (thinly laminated) and Figure 7C (thickly laminated). Mastcam images acquired on Sol 792 (left), and sol 712 (right).
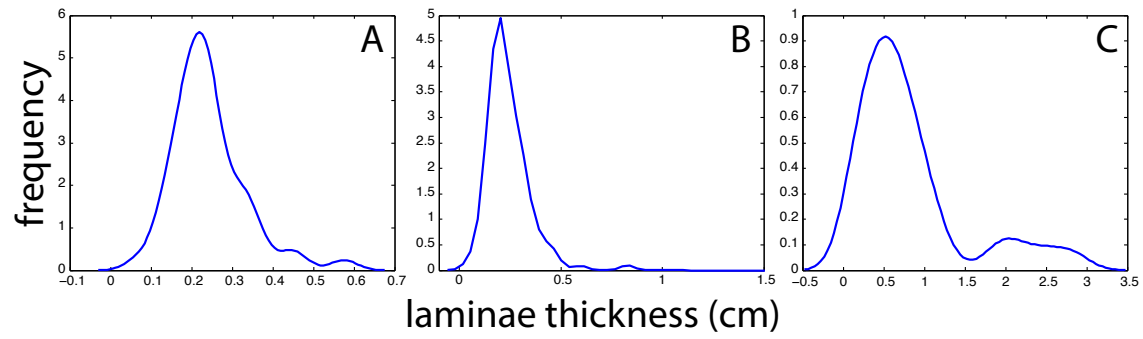
Fig. S6

Kernel density estimates of the laminae thickness distributions for the regions of interest A, B, and C shown in Figure S5.
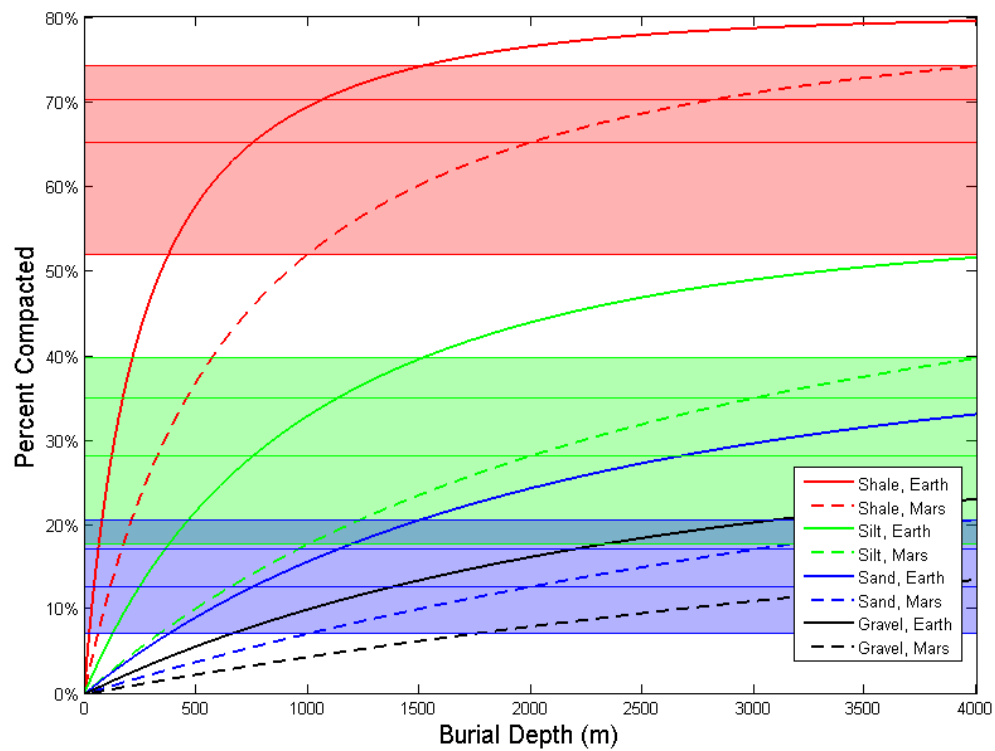
Fig. S7

Percent compaction of sedimentary layers in monolithologic column of sediments on Earth and Mars based on burial depth and lithology.
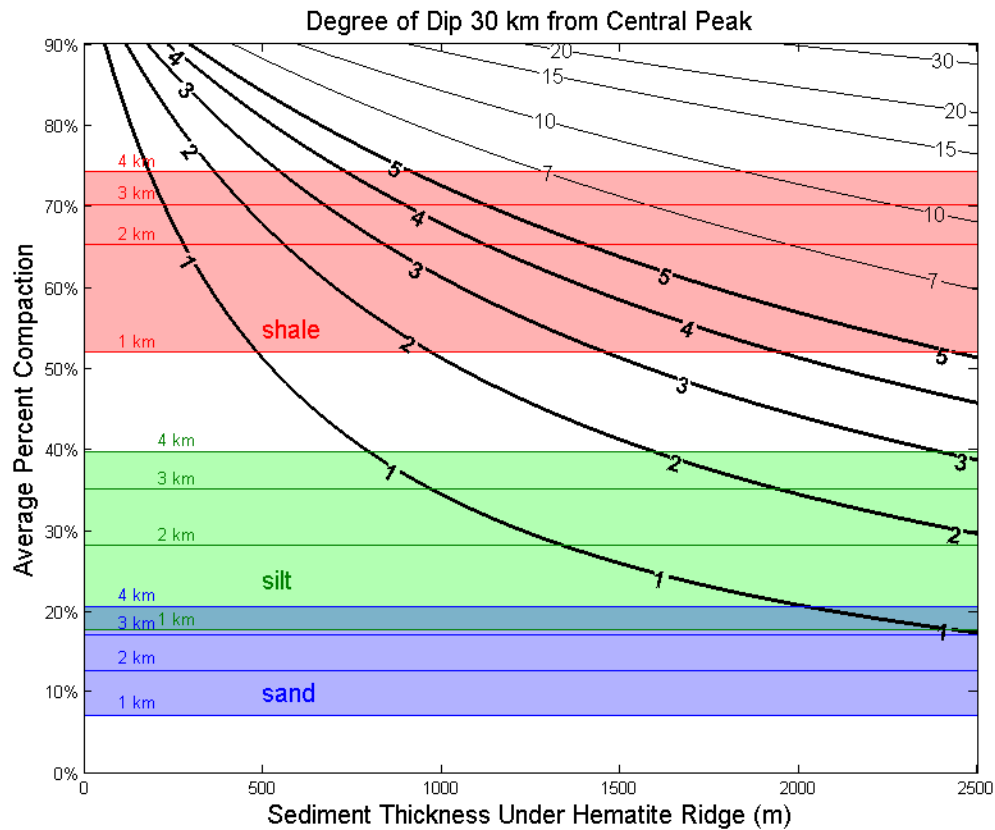
Fig. S8

Expected dip angle away from Mount Sharp as a function of sediment compaction of strata beneath the hematite ridge (estimated to be 1.2-2.2 km), and the average percent of compaction within that sediment pile (varies depending on the lithology of the sediments and amount of burial). Expected self-compaction of shale, silt, and sand under 1-4 km of sediment are shown in red, green, and blue respectively (from Figure S7). Contours are thickened for measured dips of 3°±2° (*55*).
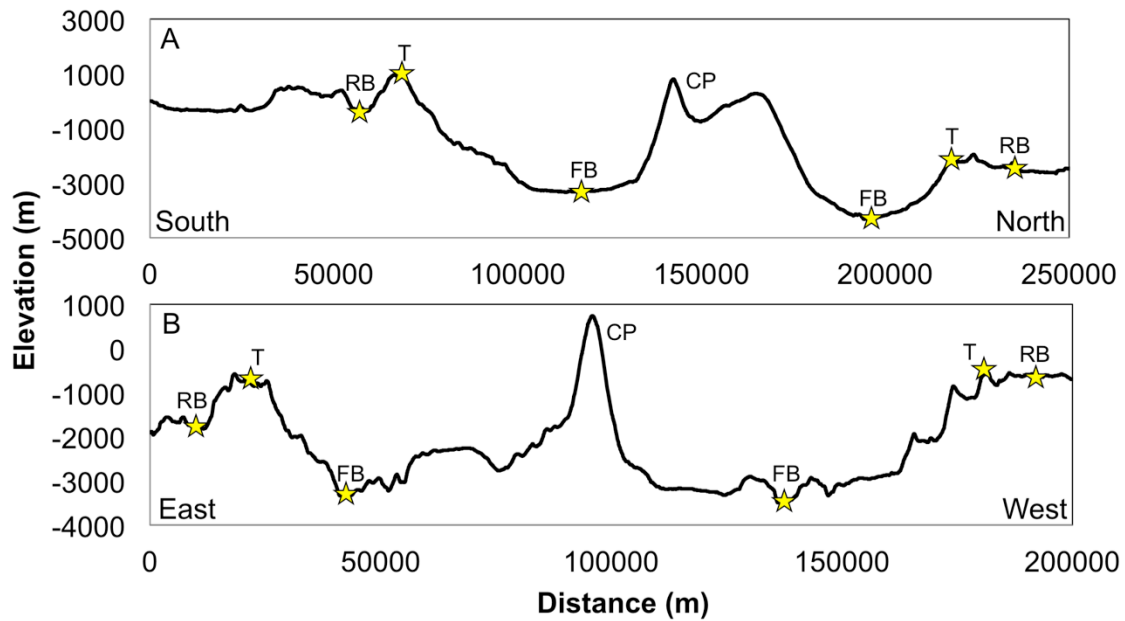
Fig. S9

A) A representative long profile across Gale Crater going from the south to the north. The yellow stars correspond to measurement locations (RB = rim bottom, T = rim top, CFB = current floor bottom, and CP = central peak), from which the crater rim height (T-RB), the rim to infilling depth (T-FB), and the crater diameter (distance between rims) were calculated (we did not include our measurements of the northern crater rim height in our erosion analysis). As Gale has a partially preserved ejecta blanket, our rim bottom locations were taken as far from the rim as possible (distances >50 km) while still avoiding neighboring crater systems. B) Representative long profile across Gale Crater going from the east to the west, where the dashed lines are derived from MOLA data and the solid line is derived from HRSC data.
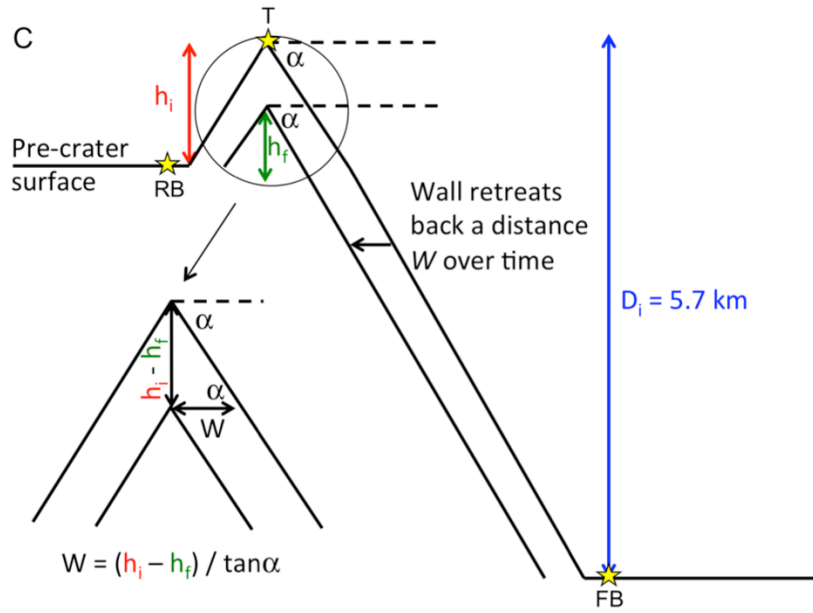
Fig. S10

Idealized crater degradation model, where hi is the initial crater rim height as calculated from the relation in Robbins and Hynek (*63*), hf the current-day crater rim height measured from our profiles, and the tangent of a gives the crater rim slope. As in Figure S9, RB = rim bottom, T = rim top, CFB = current floor bottom. To calculate the amount of backwasting, W, we take the difference between the initial crater rim height and the current-day height and divide it by the crater rim slope.

	Grain size (matrix; μm)	Grain size (entrained grains; μm)
Targets (brushed, imaging at 2 cm standoff or better available)		
Pelona - Shoemaker	< 60-70	
Ricardo - Shoemaker	< 60-70	
Mammoth - Confidence Hills	< 60-70	
Moenkopi - Confidence Hills	< 60-70	
Morrison - Confidence Hills	< 60-70	
Maturango - Confidence Hills	< 60-70	
Rosamond - Pink Cliffs	< 60-70	400-1000
Mojave - Pink Cliffs	< 60-70	600-1000
Afton Canyon - Book Cliffs	< 60-70	
Topanga-Book Cliffs	< 60-70	
Punchbowl_Book Cliffs	< 60-70	
Mescal - Alexander Hills	< 60-70	
Puente - Alexander Hills	< 60-70	
Goldstone - Chinle	< 60-70	
Pickhandle - Chinle	< 60-70	
Tecoya - Whale Rock	60-100	170-595
Sierra Nevada - Whale Rock	60-100	100-300
Santa Ana - Whale Rock	60-260	340-770

Table S1.

Grain size data for targets identified within the stratigraphic section exposed at Pahrump Hills (see Figure 7). All rocks are thinly laminated except for Whale rock which shows climbing ripple cross stratification. At the Pink Cliffs target (see Figure 7A for location) larger particles may be present, "floating" in the typically fine sediment, or these larger particles are diagenetic in origin. Grains were analyzed at a MAHLI standoff distance of 2 cm, which provides the highest resolution available of 17-22 microns/pixel.

ROI	median (cm)	μ (cm)	σ (cm)	*a*	*b*
A	0.20	0.24	0.09	7.92	0.03
B	0.20	0.24	0.11	6.28	0.04
C	0.55	0.81	0.68	1.90	0.43

Table S2.

Statistics of the laminae thickness distributions of the regions of interest shown in Figure S2. *a* and *b* are maximum likelihood estimates for gamma distribution shape and scale parameters, respectively.